THE SHAPE OF VOLCANIC CONDUITS INFERRED FROM BUBBLE SIZE DISTRIBUTIONS

Sahand Hajimirza[1*], Helge M. Gonnermann[1], and James E. Gardner[2]

[1]Department of Earth, Environmental and Planetary Sciences, Rice University, Houston, TX, USA
[2]Jackson School of Geosciences, University of Texas at Austin, Austin, TX, USA

ABSTRACT

The most intense known explosive volcanic eruptions on Earth are Plinian eruptions of silicic magma. Geospeedometers indicate that Plinian magma erupts from high pressure within the magma chamber at average speeds of 0.001-1 MPa/s . At the same time, dissolved magmatic volatiles, predominantly water, nucleate about one quadrillion bubbles per cubic meter of melt, preserved as vesicles within tephra. Vesicles span several orders of magnitude in size, with power-law size distributions, and vesicularities of approximately 70±20 vol.% . To date these combined observations of relatively modest decompression rates, a reflection of the fluid dynamics of magma ascent, as well as the exceedingly large bubble number densities with power-law size distributions, a consequence of bubble nucleation and growth kinetics, have never been explained in a quantitatively coherent manner. Here we demonstrate that the integration of these observations requires that bubble nucleation commences when magma starts ascending from within the chamber and continues until the magma fragments to produce tephra, contrary to the conventional view that nucleation occurs as a burst at high supersaturation. We substantiate experimentally that nucleation in rhyolitic melt can occur continuously over prolonged time intervals. We then use integrated modeling of bubble nucleation and fluid dynamics of magma ascent to demonstrate that bubble size distributions in Plinian pyroclasts are the product of continuous nucleation throughout magma ascent, and at average decompression rates that are consistent with geospeedometers. An important outcome of our results is that the transition from magma chamber to volcanic conduit is gradual, resembling a cupola that narrows upward into a conduit.

1 INTRODUCTION

The abundant bubbles that form during magma ascent in the conduit power explosive volcanic eruptions. The supercritical aqueous fluid within those bubbles is of lower density than the silicate melt from whence it exsolved [1, 2]. By virtue of conservation of mass the volume of magma, that is silicate melt plus bubbles, increases as it rises toward the Earth's surface. This results in magma acceleration and expansion [3, 4]. During explosive eruptions the associated strains and strain rates will cause the magma to fragment, which in turn is a defining process of explosive silicic eruptions [5, 6, 7].

Bubbles form by exsolution of volatile elements dissolved in the magma, as a consequence of decreasing magma pressure en route to the surface [8]. Volatile exsolution involves the simultaneous nucleation of new bubbles and diffusion from the melt into the existing bubbles [9, 10].Volatiles become supersaturated as magma pressure decreases, inducing bubble nucleation [8, 10, 11]. Diffusion of volatiles, in particular H_2O, from the melt into existing bubbles causes bubbles to grow [9, 10], while at the same time decreasing supersaturation and increasing magma viscosity [12]. A dynamical feedback between decompression, which increases supersaturation, and diffusion, which decreases supersaturation, ensues. This feedback controls bubble nucleation and growth rates [10, 13]. A record of these intertwined processes is the bubble size distribution (BSD), preserved in pyroclasts as the vesicle size distribution (VSD) [14, 15, 16, 17, 18, 19].

Common characteristics of VSDs from Plinian eruptions are high number densities ($\sim 10^{15\pm1}$ m^{-3}), as well as vesicle sizes with a power-law distribution across at least three orders of magnitude. Although VSDs have been interpreted in terms of bubble nucleation and growth [14, 15, 16, 17, 18, 20, 19, 21, 22, 23], which ultimately are the consequence of eruptive magma ascent, they have never been reproduced congruently within the context of the fluid dynamics of magma ascent. Moreover, existing models that predict bubble number density tend to infer magma decompression rates that are at odds with geospeedometers, which yield orders of magnitude lower decompression rates [24, 25]. Here we resolve both discrepancies using numerical modeling of eruptive magma ascent and vesiculation, with the latter encompassing bubble nucleation and growth. Our simulated BSDs reproduce observed VSDs at average decompression rates that are consistent with geospeedometers.

2 APPROACH

2.1 *Continuous nucleation*

The continuous power-law vesicle size distributions in pyroclasts are thought to be the result of protracted bubble nucleation throughout magma ascent [20, 21]. Although such continuous nucleation is in principle consistent with nucleation theory [10, 27, 28], broad VSDs as observed in Plinian pyroclasts are usually not produced in nucleation experiments [29, 30, 26]. Moreover, because it is nearly impossible to directly observe bubble nucleation during these high pressure and temperature experiments, continuous nucleation cannot be substantiated through direct observation.

The objective of our experiments is to validate that bubble nucleation during decompression of hydrated rhyolitic melt can indeed be continuous. The experiments consisted of three steps

*correspondence: sahand@rice.edu

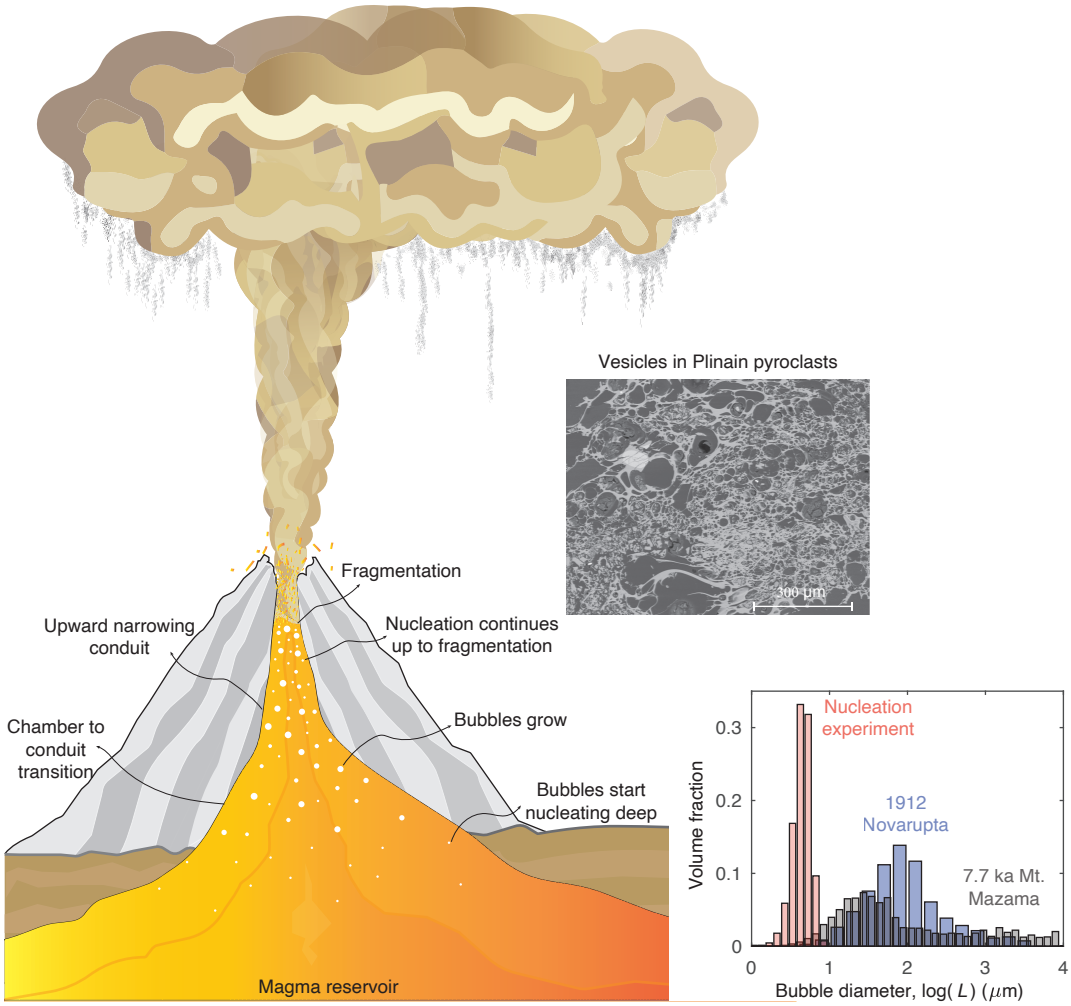

Figure 1: Schematic diagram of the magma storage-conduit system envisaged during Plinian eruptions. Bubbles begin nucleating during magma withdrawal within the upper reaches (cupola) of the magma reservoir. Nucleation continues up to the point of magma fragmentation. Bubble size distributions, preserved in Plinian pyroclasts, are produced by a continuous and protracted nucleation process. Inset: scanning electron microscope image of air-fall pumice from the 7.7 ka Plinian eruption of Mt. Mazama, Oregon (courtesy T. Giachettii), and a comparison between VSD in Plinian pyroclasts and in nucleation experiments [26]. Data for eruptions are a composite VSD of Plinian fall deposits from 1912 Novarupta [15] and 7.7 ka Mt. Mazama [14] eruptions.

[31] (Supplementary Table 1; Supplementary Figure 1). First samples were hydrated at an initial pressure, P_i = 160-250 MPa, and temperature, T = 850 °C, until equilibrium was achieved. Next, samples were decompressed over a time interval, 1 s $\leq t_d \leq$ 50 s, to their final pressure, P_f = 10-100 MPa. In the final step, samples were held at the final pressure for an annealing time of 0 s $\leq t_{post} \leq$ 120 s, and then were rapidly quenched. Bubble number density was subsequently measured in thin sections of the quenched samples. The experiments were divided into six suites for each of which saturation pressure, decompression rate, and final pressure were closely similar. Within each suite samples were quenched at different t_{post}. If nucleation was ongoing during the annealing period, then samples within a given suite should have a positive correlation between t_{post} and bubble number density.

2.2 *Modeling of magma ascent and bubble nucleation*

We simulate the fluid dynamics of eruptive magma ascent, together with bubble nucleation and growth during Plinian eruptions, as illustrated conceptually in Figure 1 (see Methods for details). We assume a cylindrical conduit whose radius may vary with depth and solve the steady mass and momentum conservation equations for the change in magma velocity and pressure with depth. The latter provides the boundary condition for the integrated bubble nucleation and growth model. We only consider H_2O, the most abundant volatile phase [32] and driver of bubble nucleation [8, 10], and we assume heterogeneous nucleation [24, 25]. Our objective is to test the hypothesis that VSDs in Plinian pyroclasts are the product of continuous nucleation during magma ascent. Each simulation is therefore constrained to maintain sufficient supersaturation for nucleation. This is achieved by varying conduit size, such that at any given depth the magma decompression rate is slightly greater than the in-

verse characteristic diffusion time. Conceptually this approach is similar that employed in conduit models with a near-lithostatic magma pressure [33]. Thus, aside from predicting decompression rate, bubble number density and size distribution, the model also predicts conduit radius as a function of depth.

3 RESULTS

3.1 *Experimental verification of continuous bubble nucleation*

Our experiments produced bubble number densities that vary over 5 orders of magnitude (10^8-10^{13} bubbles per m^3 of melt). Although supersaturation, defined as the difference between the initial and final pressures, drives nucleation, experimental BNDs are not correlated with supersaturation (Supplementary Figures 1 and 2). Instead, experiments within a suite produced BNDs that vary by up to 2 orders of magnitude and are correlated with the annealing time, t_{post}.

Because BNDs among various suites vary significantly, a synthesis of all experiments requires non-dimensionalization of bubble number density and annealing time. t_{post} is scaled by the nucleation time scale, τ, which represents the time that nucleation rate drops by one e-folding time. Bubble number density N_{post} is non-dimensionalized by N_{eq}, the final bubble number density that a sample could theoretically have attained. For each experimental suite N_{eq} and τ are estimated by minimizing the difference between predicted (equation 33) and observed bubble number densities (Supplementary Figure 3). The resultant values are similar for samples within a given experimental suite and predominately depend on the initial and final pressures (Supplementary Table 2). Non-dimensional BND is predicted to increase linearly between $0 \leq t_{post} \leq \tau$, after which it reaches its maximum value [27]. Thus, non-dimensionalization should collapse all experiments during which nucleation was continuous onto the black line shown in Figure 2, which is the case within the expected experimental variability. Given that the maximum value of τ in our experiments was ≈1000s, our experiments indicate that bubble nucleation in rhyolitic melt can be a continuous process for at least that long.

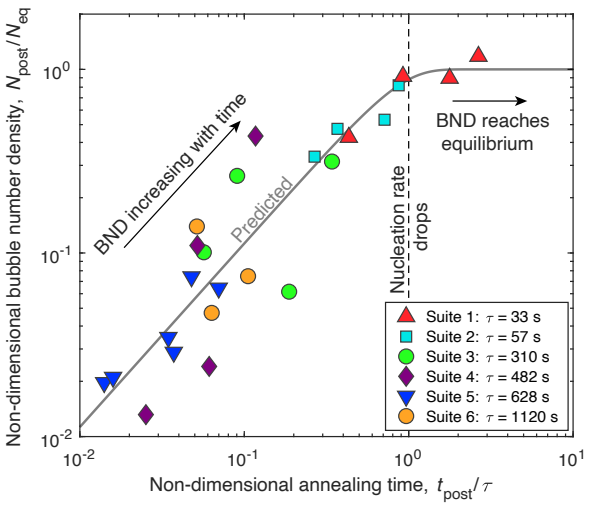

Figure 2: Continuous bubble nucleation in decompression experiments. Data are represented in non-dimensional variables. The sample annealing time is non-dimensionalized by the nucleation time scale, τ. Bubble number density is non-dimensionalized by the equilibrium value of the given sample suite, N_{eq} (Equation (36)). The values of τ and N_{eq} are constant for each experimental suite (Table S2). All experiments fall along the trend expected for continuous nucleation (Equation (33)), demonstrating that that bubble nucleation in rhyolitic melts is continuous across a wide range in conditions. Given the range of τ in our experiments, nucleation was continuous for at least 1000 seconds.

3.2 *Key results for bubble nucleation during magma ascent*

Figures 3 and 4 show simulation results for a typical Plinian discharge rate of $Q = 5 \times 10^7$ kg/s and an initial H_2O saturation at a pressure of 145 MPa, typical values for Plinian eruptions [3]. We assume choked flow at the surface [33, 34], and similar results are obtained for different discharge rates and/or saturation pressures. To examine the effect of bubbles that had formed prior to an eruption on bubble nucleation [35, 36], we simulated a case with no initial bubbles (shown in blue) and a case with an initial volume fraction of 0.03 bubbles (shown in red). The simulations shown in thick blue and red lines were obtained by adjusting conduit radius such that the decompression rate is greater than the inverse characteristic H_2O diffusion time at all depths above where the first bubbles nucleate (for more details see equation (30) in Methods). In other words, the resultant conduit radius gives decompression rates at which supersaturation and nucleation are maintained throughout magma ascent. No other parameters were adjusted to obtain the simulation results shown. Figure 4 shows the modeled BSDs together with VSDs in pyroclasts from several Plinian eruptions. The close match is strictly a model outcome of continuous nucleation. It is not a consequence of 'tuning' model simulations to achieve a match. For all cases shown, the match between predicted bubble size distributions and those measured in Plinian pyroclasts is remarkable and suggests that bubble nucleation during eruptions is indeed continuous throughout magma ascent, presumably commencing shortly above the magma chamber or perhaps already during magma withdrawal from the chamber.

The thin blue and red simulations illustrate model sensitivity to variations in predicted conduit radii, relative to the two base cases for which conduit radius was constrained to assure continuous nucleation. Conduit radii were shifted to smaller and larger values relative to the base cases. The key result is an upward narrowing conduit is necessary for continuous nucleation. Variations in conduit radius primarily affect decompression rate, fragmentation depth, and bubble number density, but still yield results for all relevant parameters that are well within range of observed or inferred values for Plinian eruptions. At very low nucleation rates ($J < 10^9$ m^{-3} s^{-1}) nucleation is quite sensitive to small variations in conduit radius (decompression rate), resulting in oscillations in nucleation rate. These, however, quickly dampen as bubble number densities, N_m exceed values of 10^{10} bubbles per m^{-3} of melt.

3.3 *Eruption dynamics*

As bubbles nucleate and grow, the distance between bubbles decreases. Consequently the characteristic diffusion rate, which scales as the inverse squared distance between bubbles, increases.

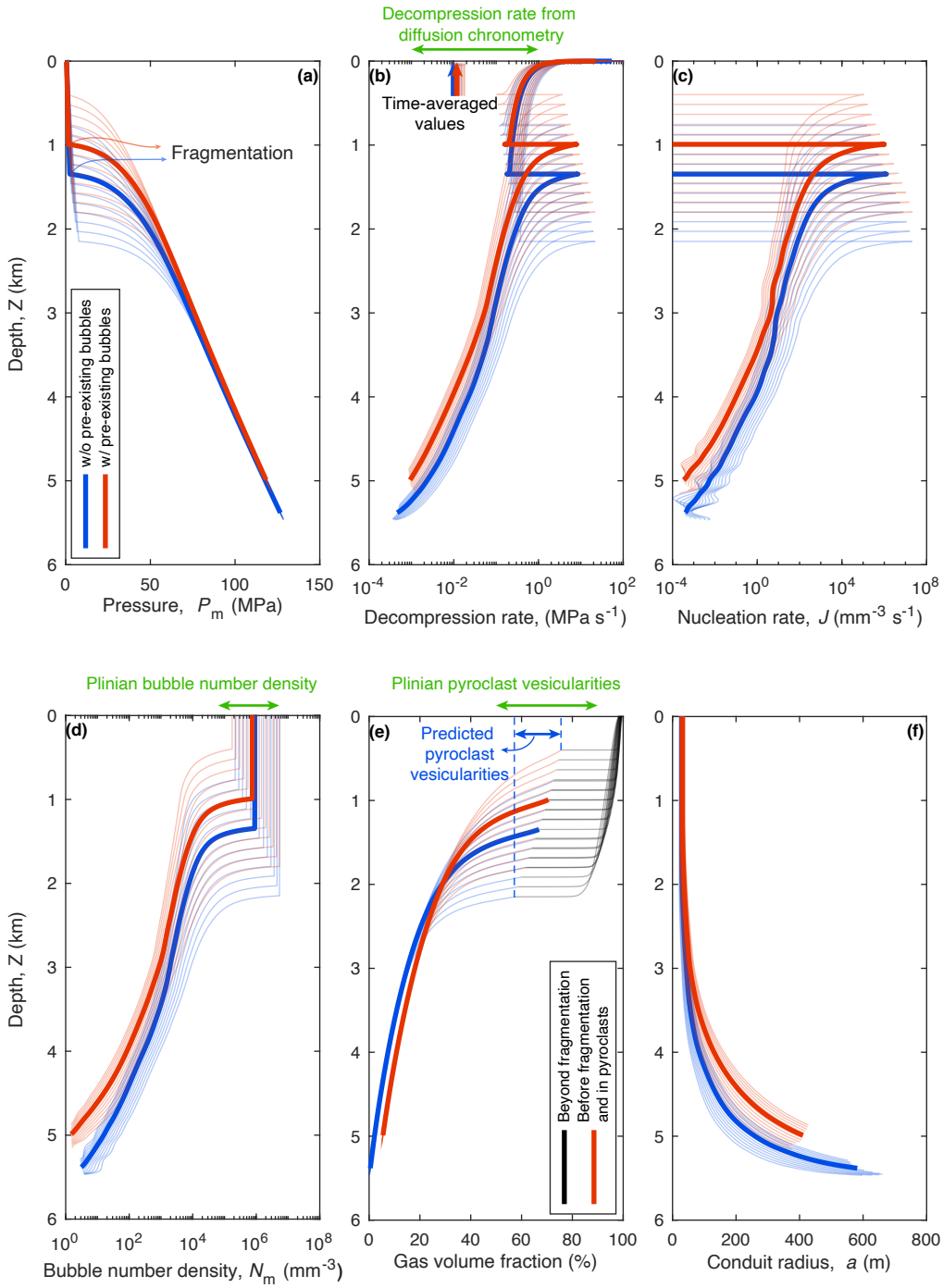

Figure 3: Simulation results for a mass discharge rate of 5×10^7 kg/s and H_2O saturation pressure of 145 MPa. The blue and red curves represent simulations with three percent and without pre-existing bubbles, respectively. The results are shown from nucleation onset until magma reaches the surface. **(a-b)** Pressure decreases as magma ascends, due to hydrostatic and viscous pressure loss. **(c)** As a consequence H_2O becomes supersaturated, causing heterogeneous bubble nucleation. **(d)** Consequently bubble number density increases as magma ascends to shallower depths. **(e)** Nucleation, in conjunction with diffusion of H_2O into existing bubbles, as well as decompression of the fluid inside bubbles, results in an increase of volume fraction of exsolved H_2O. **(a-e)** At the depth of magma fragmentation there is an abrupt change in the trend of the aforementioned variables. **(f)** Conduit radius as a function of depth required to obtain continuous nucleation during magma ascent.

To maintain supersaturation and nucleation, decompression rate has to accelerate with distance above the magma reservoir. This acceleration is in part due to the upward narrowing conduit. Together with bubble nucleation and growth, it increases the

average magma velocity, which in turn increases the viscous pressure loss. At the same time and also due to bubble nucleation and growth, the average water concentration within the melt decreases, which increases magma viscosity and further enhances the viscous pressure loss. Eventually this results in a runaway feedback between decompression rate, water exsolution and viscosity. In Figures 3a and 3b this manifests itself as the pronounced curvature in P_m and decompression rate prior to fragmentation. The rapidly accelerating decompression rate results in increasing supersaturation and therefore an increasing nucleation rate (Figure 3c). At the same time bubble number density and volume fraction of bubbles also increase (Figures 3d & e). Once the feedback between decompression rate, water exsolution and viscosity becomes dominant the conduit radius no longer needs to decrease in order to maintain supersaturation (Figure 3f). Instead, it is this runaway feedback that produces the high overall bubble number density. The shift in dynamics due to the feedback is associated with the small diameter tail in the bubble size distribution, which can also be found in Plinian VSDs, where it is associated with a decrease in the power-law exponent of the distribution (Figure 4).

Upon fragmentation gas pressure inside bubbles quickly equalizes with magma pressure. This is a consequence of permeable gas flow from pyroclasts into the surrounding fractures. It produces a rapid increase in gas volume fraction as the gas-pyroclast mixture expands (Figure 3e). Outgassing of the pyroclasts is simulated using a pore-pressure relaxation rate (equation (23) in Methods), using pyroclast permeabilities [37]. At the same time decompression rate decreases, because of the abrupt change in viscosity, which is much lower for the gas-pyroclast mixture above fragmentation than for the bubbly magma (Figure 3b). As a consequence there is rapid water diffusion out of the melt and loss of supersaturation conditions. H_2O continues to exsolve from the melt inside the pyroclasts en route to the surface, contributing together with the expansion of the exsolved H_2O to the continued increase in gas volume fraction (Figure 3e). The mixture of gas-pyroclasts thus accelerates and reaches choked flow conditions at the conduit exit [3, 33, 38]. We assume that bubbles do not nucleate and grow within the pyroclasts after fragmentation. In other words, any remaining dissolved H_2O exsolves through diffusion into existing bubbles and then enters the gas phase that surrounds pyroclasts by permeable flow within the pyroclasts [39].

4 Discussion

Continuous nucleation reconciles multiple observations from Plinian eruptions. When such nucleation is incorporated into numerical models for eruptive magma ascent the predicted bubble number number densities and vesicularities are within the range of Plinian pyroclasts (Figure 3). Moreover, the predicted BSDs also mirror those measured in Plinian pyroclasts (Figure 4). They span several orders of magnitude in size. In addition, the observed change in power-law exponents from d = 3-4 to d = 1-2 with decreasing vesicle size [15, 19, 16, 14] is also present in the simulated BSDs. This change in slope of the size distribution can be attributed to the aforementioned accelerating feedback between viscous pressure loss and nucleation. Although magma decompression rate increases continuously as magma rises toward the level of fragmentation, the predicted

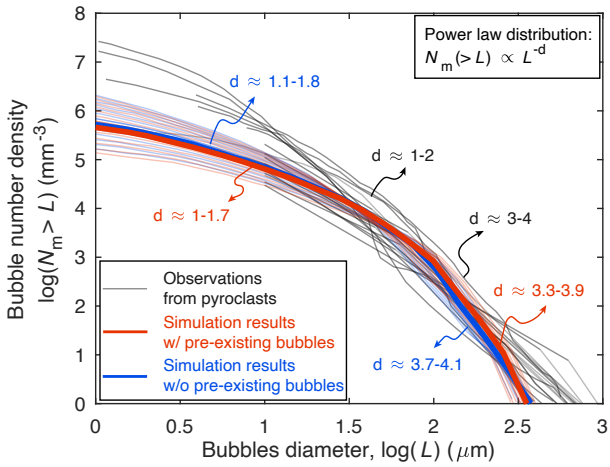

Figure 4: Simulated bubble size distributions corresponding to the simulations of Figure 3 (red and blue curves), together with distributions from Plinian pyroclasts (gray curves). The latter are from the 1912 Novarupta eruption in Alaska[15], the 1875 Askja eruption in Iceland[16], the 2008 Chaiten eruption in Chile[19], and the 7.7 ka Mazama eruption, Oregon[14]. Plinian BSDs have been subdivided into two overlapping power law distributions with exponents of $d \approx$ 3-4 and $d \approx$ 1-2. In the simulations the latter size fraction of the distribution represents bubbles nucleated during the rapid increase in decompression rate in the depth range where the feedback between water exsolution and viscous pressure loss accelerates up to fragmentation.

time-averaged decompression rates $\sim 10^{-2}$ MPa s^{-1} are well within the 0.001 – 1 MPa s^{-1} range of diffusion chronometers [40]. Thus, continuous nucleation fully closes the large previous gap in decompression rate estimates between diffusion chronometers and bubble nucleation models [24, 40].

An interesting result is the apparent necessity that conduits widen with depth from a few 10s of m at shallow depths to radii of 100s of m at H_2O saturation depths. One may view our simulated 'conduits' as cupolas at the top of magma chambers, narrowing upward into a developing conduit [41]. The implication would be that bubbles start nucleating within the upper reaches of the magma chamber during magma withdrawal, and the resultant decompression rates span a wide range in values [42]. Motivated by this consideration we also examined the role of pre-existing bubbles prior to eruption [35, 36] and find that they do not effect the essence of our simulation results.

4.1 *Conclusion*

We have demonstrated experimentally that bubble nucleation in rhyolitic melt can be a continuous process over time intervals of at least thousands of seconds. Building upon this insight, numerical simulations of bubble nucleation and growth, in conjunction with the fluid dynamics of eruptive magma ascent, demonstrate that vesicle size distributions in Plinian pyroclasts can be explained by continuous bubble nucleation during magma ascent. The ensuing average magma decompression rates are consistent with diffusion-chronometry geospeedometers. Moreover, the resultant bubble size distributions are similar to vesicle size distributions measured in Plinian pyroclasts, regardless of whether

or not some bubbles already exist in the magma prior to eruption. A necessary condition is that conduits widen with depth and transition via a broad cupola into the upper reaches of magma reservoirs.

5 METHODS

We model the one-dimensional fluid dynamics of steady magma flow in the volcanic conduit, coupled with the nucleation and growth of H_2O bubbles. Simulations start at H_2O saturation, corresponding to a pressure, P_{H_2O}. Assuming a constant lithostatic pressure gradient of $\rho_{rock}g$, where $\rho_{rock} = 2400$ kg/m^3 is rock density and g is gravity acceleration, the saturation pressure P_{H_2O} corresponds to a depth, $Z_0 = P_{H_2O}/(\rho_{rock}g)$. Simulations end when magma reaches the surface at $Z = 0$. As magma flows up the volcanic conduit magma pressure, P_m, decreases due to hydrostatic and viscous pressure loss. The magma thus becomes supersaturated in H_2O, resulting in bubble nucleation. At the same time H_2O diffuses from the melt into existing bubbles, as they grow. The fluid dynamics of magma ascent are coupled with the nucleation and growth of bubbles through magma pressure P_m, which provides a depth-varying boundary condition for the bubble nucleation and growth calculations. In the subsequent sections we will detail the methodologies for employed to model magma flow in the conduit as well as bubble nucleation and growth within the ascending magma.

5.1 *Magma flow in the conduit*

We assume a vertical cylindrical conduit, whose radius can vary with depth, Z. We assume the flow is steady because the duration of magma ascent is much shorter than the duration of Plinian eruptions [43]. We assume flow is one dimensional and integrate flow properties over the cross-sectional area of the conduit. Below the level of fragmentation we define magma as the mixture of silicate melt and H_2O bubbles. Above the level of fragmentation magma is the mixture of continuous H_2O vapor with suspended fragments of vesicular magma, that is pyroclasts. Throughout the relative velocity between the two phases (melt and H_2O vapor/fluid) is neglected. Below fragmentation this is justified because the buoyant rise velocity of bubbles is negligible, given the large melt viscosity [33]. Above fragmentation it is a commonly employed approximation [3, 33] and one that does not affect the salient results of our simulations in any significant manner. The properties of the mixture, that is of the magma, are the volumetric average of the two phases. The flow is furthermore assumed to be isothermal, another common approximation that dose not significantly impact bubble nucleation rate [38].

With these assumptions, conservation of mass and momentum are [3, 33]

$$\frac{\partial(\rho_m u A)}{\partial z} = 0, \tag{1}$$

and

$$\rho_m u \frac{\partial u}{\partial z} = -\frac{\partial p_m}{\partial z} - \rho_m g - F_{fric}, \tag{2}$$

respectively. Here ρ is magma density, averaged over liquid and gas phases,

$$\rho = \phi\rho_g + (1-\phi)\rho_l. \tag{3}$$

ϕ is the volume fraction of bubbles, u is magma ascent rate, $A = \pi a^2$ is the conduit cross sectional area, a is conduit radius, and ρ_g and $\rho_l = 2400$ kg/m^3 are gas and melt densities respectively. F_{fric} is the frictional pressure loss estimated as $\rho_m u^2 f/a$ where f is the friction factor. Before fragmentation $f = 16/Re + f_0$ and after fragmentation $f = f_0$. $Re = 2\rho_m ua/\eta$ is the Reynolds number, η is the viscosity of the mixture, and f_0 is a factor related to conduit wall's roughness and assumed to be 0.0025 [33].

By substituting equation (1) into (2) one obtains

$$-\frac{\partial p_m}{\partial z} = \rho_m g + F_{fric} - \frac{\rho_m u^2}{A}\frac{\partial A}{\partial z} - u^2\frac{\partial \rho_m}{\partial z}. \tag{4}$$

Here

$$\frac{\partial \rho_m}{\partial z} = \frac{\partial \rho_m}{\partial p_m}\frac{\partial p_m}{\partial z}, \tag{5}$$

and given that under constant entropy

$$\frac{\partial \rho_m}{\partial p_m} = c^2, \tag{6}$$

where c is the speed of sound within the magma. Equation (4) can thus be simplified to

$$-\frac{\partial p_m}{\partial z} = \frac{\rho_m g + F_{fric} - \frac{\rho_m u^2}{A}\frac{\partial A}{\partial z}}{1 - M^2}, \tag{7}$$

where $M = u/c$ is the Mach number of the mixture. The sound speed before fragmentation is estimated from $c^2 = K_m/\rho_m$ where K_m is bulk modulus of the mixture

$$\frac{1}{K_m} = \frac{\phi}{K_g} + \frac{1-\phi}{K_l}. \tag{8}$$

The bulk modulus of the gas phase, K_g, is calculated from equation of state [2] and the liquid is assumed to be incompressible [38]. The sound speed of the gas-pyroclast mixture after fragmentation is assumed to be equivalent to the sound speed in the gas phase [34]. Alternate models for the sound speed of the gas-pyroclast mixture [33] do not affect the outcome of the model results in terms of bubble nucleation, which occurs prior to fragmentation.

5.2 *Bubble nucleation and growth*

We assume H_2O is the only volatile phase because it is most abundant and controls final bubble number density [32]. H_2O exsolves through bubble nucleation and diffusion into already nucleated bubbles. We assume nucleation is heterogeneous and facilitated by abundant pre-existing magnetite nanolites [24, 25]. We use the far field approximation to calculate H_2O diffusion from melt into bubbles [10]. Lastly, we assume that permeable escape of H_2O vapor from the bubbles is negligible before magma fragments, but account for it after fragmentation. The bubble nucleation and growth model is in the Langrangian frame of reference. It is integrated to the steady state equations for magma flow in the conduit, which is in Eulerian frame of reference, by considering $d/dt = u\partial/\partial z$.

The number of bubbles in volcanic systems is too high to track growth of each individual bubble. We therefore use the method of moments to calculate the evolution of the bubble population [10]. The corresponding moments of the population, μ, are defined as

$$\mu_k(t) = \int_0^\infty R^k \Lambda(R,t)\, dR, \tag{9}$$

where R is the bubbe radius, $\Lambda(R,t)$ is the bubble population per unit volume of melt within the interval of R and $R+dR$, and subscript k = 0-3 refers to the order of the moment. Each moment refers to a measurable characteristic quantity [10]. μ_0 is the bubble number density, that is the number of bubbles per unit volume of melt, μ_1 is the sum of bubbles radius, $4\pi\mu_2$ is the total surface area of bubbles, and $4/3\pi\mu_3$ is the total volume of bubbles. The evolution of moments through time is given by

$$\frac{d\mu_0}{dt} = J, \tag{10}$$

and for , k $\geq$ 1, by

$$\frac{d\mu_k}{dt} = kG(\hat{R})\mu_{k-1} + JR_c^k, \tag{11}$$

where J is nucleation rate of bubbles, $G(\hat{R})$ is the growth rate of bubbles assumed to be equal for all bubbles and equivalent to the growth rate of a bubble with mean bubble size, $\hat{R} = \mu_1/\mu_0$, and R_c is the critical size for nucleating bubbles.

5.2.1 *Below fragmentation*

We use classical nucleation theory to estimate nucleation rate of stable bubble nuclei as a function of supersaturation pressure. Nucleation rate of stable bubbles are [11]

$$J = J_0 \exp\left(-\frac{W}{k_B T}\right), \tag{12}$$

and bubbles are stable if they are larger than a critical size, R_c, given by

$$R_c = \frac{2\gamma}{p_n - p_m}. \tag{13}$$

Here T is the absolute temperature, k_B is the Boltzmann constant, γ is the surface tension of bubble nuclei, P_n is the pressure inside a bubble nucleus, and P_m is pressure in the mixture. p_n is related to the saturation pressure of volatiles, p_{sat}, through [44]

$$f(p_n, T)p_n = f(p_{sat}, T)p_{sat}e^{\Omega(p_m - p_{sat})/k_B T}, \tag{14}$$

where $f(p, T)$ is the fugacity coefficient, and Ω is the volume of volatile molecules. W is the change in free energy as a result of nucleation of a bubble and is given by

$$W = \frac{16\pi\gamma^3}{3(p_n - p_m)^2}\alpha, \tag{15}$$

where α is the heterogeneous nucleation factor and depends on the contact angle, θ, between bubble nuclei and pre-existing crystals. It is defined as

$$\alpha = \frac{(2 - \cos\theta)(1 + \cos\theta)^2}{4}, \tag{16}$$

and we assume nucleation is facilitated by magnetite crystals with $\theta = 145°$ [45, 46].

The pre-exponential factor, J_0, in equation (12) is defined as

$$J_0 = \frac{2\Omega n_0^2 D}{a_0}\sqrt{\frac{\gamma}{k_B T}}, \tag{17}$$

where n_0 is the concentration of volatiles molecules in the melt, D is the diffusion coefficient, a_0 is the average distance between volatiles molecules.

After nucleation bubble nuclei grow by H_2O diffusion, because the concentration of H_2O at the bubble-melt interface, C_R, is lower that the concentration in the surrounding melt, C_m. The H_2O flux into bubbles is given by

$$q = D\left(\frac{\partial c}{\partial r}\right)_{r=R}, \tag{18}$$

where D is diffusion coefficient, r is the distance from bubble's center, R is bubble radius, and c is the water concentration in the surrounding melt given by

$$\frac{\partial c}{\partial t} + \frac{dR}{dt}\frac{\partial c}{\partial z} = \frac{1}{r^2}\frac{\partial c}{\partial r}\left(Dr^2\frac{\partial c}{\partial r}\right). \tag{19}$$

At low supersaturation pressure the left hand side in equation (19) can be neglected [47]and the concentration gradient at the melt-vapor interface can be approximated as

$$\left(\frac{\partial c}{\partial r}\right)_{r=R} = \frac{C_m - C_R}{R}. \tag{20}$$

The mass of H_2O inside bubbles, m_g, will increase due to diffusion at a rate

$$\frac{dm_g}{dt} = (4\pi\mu_2)\rho_m q, \tag{21}$$

whereas the bubble growth rate is given by [48]

$$G(\hat{R}) = \frac{\hat{R}}{4\eta}\left(p_g - p_m - \frac{2\gamma}{\hat{R}}\right), \tag{22}$$

where the inertia terms are neglected [10]. Here η is the viscosity of melt, p_g is the pressure the H_2O fluid (vapor) inside bubbles, estimated using the equation of state for H_2O.

5.2.2 *Above fragmentation*

After fragmentation we assume bubbles that bubbles no longer nucleate or grow [39]. In other words, $J = 0$ and $G(\hat{R}) = 0$. H_2O, however, continues to exsolve into bubbles with a rate given by equation (18). Exsolved H_2O escapes by permeable flow from within the pyroclasts into the gas phase surrounding the pyroclasts. Consequently, the gas pressure within pyroclasts decreases at a rate of

$$\frac{dp_g}{dt} = \frac{p_m - p_g}{\tau_k}, \tag{23}$$

where τ_k is the characteristic time scale for permeable outgassing estimated from Darcy's law as

$$\tau_k = \frac{l^2}{k/(\eta_g\beta\phi)}. \tag{24}$$

Here $l \approx 10$cm is the characteristics length scale [39], $k \approx 10^{-12}$m^2 is permeability [37], $\eta_g = 10^{-5}$ Pa.s is viscosity of the gas phase, and β is the compressibility of the gas phase, and ϕ is porosity of bubbles in the pyroclasts.

Lastly, the concentration of dissolved H_2O and thus the saturation pressure, both below and above fragmentation, decrease as a result of the diffusion of water into bubbles. The resultant conservation of H_2O requires that

$$\frac{dp_{sat}}{dt} \propto \frac{dC_m}{dt} = -\frac{1}{\rho_l}\left(M_0\frac{dm_g}{dt} + Jm_c\right), \tag{25}$$

where ρ_l is the melt density, assumed to be constant throughout magma decompression, and m_c is the mass of a bubble nuclei estimated from equation of state.

5.3 *Model simulation*

The parameters in the governing system of equations are either specified or calculated from existing formulations: H_2O solubility [49], diffusion coefficient [50], equation of state [2], fugacity coefficient [2], surface tension [28], melt viscosity [12], and the molecular volume of H_2O [1]. For a given simulation we integrated equations (7), (10), (11) for $k = 1$ through 3, as well as equations (23) and (25) using the `ode15s` function of MATLAB®. The boundary condition at the initial depth, z_0, are

$$\begin{aligned} p_m(z_0) &= \rho_r g z_0, \\ C_m(z_0) &= C_{eq}(p_m(z_0)), \\ \mu_k(z_0) &= N_0 R_0^k. \end{aligned} \tag{26}$$

Here $\rho_r = 2400$ kg/m^3 is the rock density, C_{eq} are the equilibrium water concentration, and N_0 and R_0 are the number density and radius of pre-existing bubbles. The boundary conditions at the surface are

$$\begin{aligned} p_m(z = 0) &= p_{atm}, \\ &\text{or} \\ M(z = 0) &= 1. \end{aligned} \tag{27}$$

We assume magma fragments at a critical porosity, ϕ_{cr}. For each simulation run, we vary ϕ_{cr} to meet the boundary condition at the surface. We estimate bubble size distribution for each simulation by post-processing the simulation results. We discretize z into multiple bins and estimate number of bubbles nucleated at each bin as

$$N_m(\bar{z}) = \int_{\bar{z}}^{\bar{z}+d\bar{z}} \frac{J}{u} dz. \tag{28}$$

and the final size of bubbles nucleated at each bin as [38]

$$L_m(\bar{z}) = 2\left(R_c(\bar{z}) + \int_{\bar{z}}^{0} \frac{G(\hat{R})}{u} dz\right). \tag{29}$$

The objective of our model is to find conditions at which bubble nucleation is continuous from nucleation onset until magma fragmentation. Nucleation is driven by supersaturation pressure, $p_{sat} - p_m$ and is thus controlled by the competition between decompression rate, dp_m/dt and dp_{sat}/dt. The latter is proportional to the diffusion rate and is estimated from equation (25). To maintain sufficient supersaturation for nucleation, we assume that the decompression rate at any given depth is greater than diffusion rate, that is

$$\left(\frac{dp_m}{dt}\right)\left(\frac{dp_{sat}}{dt}\right)^{-1} = \lambda, \tag{30}$$

where $\lambda > 1$ is a constant. This approach requires that $dp_{sat}/dt > 0$, that is sufficient number of bubbles are nucleated, to be able to estimate decompression rate. We use equation (30) at minimum bubble number density of 1 mm^{-3}. From decompression rate we estimate conduit cross sectional area, dA/dz from equation (7) analogous to the approach in Mastin and Ghiorso [33]. After finding an initial conduit radius we used the MATLAB® `pchip` function to smooth the obtained function and assess the sensitivity of model predictions to variations in conduit radius.

5.4 Nucleation time scale in experiments

Bubble nucleation is driven by supersaturation pressure, $\Delta P_{ss} = P_{sat} - P$, defined as the difference between pressure at which H_2O would be saturated and the sample's pressure, P. ΔP_{ss} increases as P decreases. Considering that diffusion is ineffective during decompression [28], P_{sat} is expected to remain the same as the initial pressure, P_i, throughout decompression. ΔP_{ss} thus reaches the maximum potential supersaturation pressure when sample pressure reaches the final pressure, $\Delta P_{ss} = \Delta P_{max}$, Supplementary Figure 1. Consequently, the nucleation rate in the experiments is expected to increases as sample pressure decreases toward P_f, because $\Delta P_{ss} \approx \Delta P$ and nucleation rate scales as $\exp(-1/\Delta P_{ss}^2)$ [11]. Nucleation rate reaches a maximum value at P_f and nucleation continues at this rate until the sample is quenched, unless at some point diffusion becomes non-negligible. Thus, the majority of bubbles are expected to nucleate once ΔP has reached its maximum $\Delta P_{max} = P_i - P_f$. If (and once) enough bubbles have nucleated to decrease the characteristic diffusion time to the point where water diffusion into existing bubbles becomes non-negligible, then $\Delta P_{ss} < \Delta P_{max}$ and nucleation rate decreases.

We used the nucleation model described in Yamada et al. [27] to quantify nucleation rate during samples hold time from observed bubble number densities. The model was obtained by analytical solution of bubble nucleation and growth formulations described in Toramaru [10]. Nucleation rate, $J(t)$, as a function of time is given by

$$J(t) = J_s \exp\left(-(t/\tau)^{5/2}\right). \tag{31}$$

Here t is time at the final pressure, J_s is the steady nucleation rate and τ is the nucleation time scale, which is the e-folding time of nucleation. τ_n scales inversely with J_s as [27]

$$\tau = k_\tau \times J_s^{-2/5}. \tag{32}$$

The coefficient k_τ depends on melt properties, in particular the diffusion coefficient. Here we assume it is constant because the variability of k_τ across the conditions of our experiments is relatively weak [27].

Integration of $J(t)$ through time yields the bubble number density that are nucleated during annealing time as a function of time, $\hat{N_{post}}(t)$, given by

$$N_{post}(t) = \int_0^t J(t')dt' = \Gamma\left(\frac{7}{5}\right) J_s\, \tau\, \Gamma\left(\frac{2}{5}, (t/\tau)^{5/2}\right), \tag{33}$$

$N_{post} = N_m + N_0$ is related to observed bubble number densities where N_0 is the bubble number density at time $t = 0$. In our experiments N_0 accounts for bubbles that were nucleated during decompression and is obtained for each suite from N_m in samples with $t_{post} = 0$. Furthermore, $\Gamma(x)$ is the gamma function

$$\Gamma(x) = \int_0^\infty z^{x-1} e^{-z} dz, \tag{34}$$

and $\Gamma(s, x)$ is the normalized lower incomplete gamma function,

$$\Gamma(s, x) = \frac{1}{\Gamma(s)} \int_0^x z^{s-1} e^{-z} dz, \tag{35}$$

Both $\Gamma(x)$ and $\Gamma(s, x)$ arise out of the integration of $J(t)$ (Equation 31).

At the nucleation time scale, $t \gg \tau_n$, nucleation rate decreases and bubble number density eventually reaches the equilibrium value of

$$N_{eq} = N_{post}(t \to \infty) = \Gamma\left(\frac{7}{5}\right) J_s\, \tau. \tag{36}$$

Lastly, the predicted non-dimensional bubble number density is estimated from equations (33) and (36)

$$\frac{N_{post}(t)}{N_{eq}} = \Gamma\left(\frac{2}{5}, (t/\tau)^{5/2}\right). \tag{37}$$

ACKNOWLEDGEMENTS

This material is based upon work supported by the National Science Foundation grants EAR-1348072 and EAR-1348050.

AUTHOR CONTRIBUTION

S.H. carried out the numerical simulations. J.E.G did the experiments. S.H., H.M.G. and J.E.G. involved in interpretation of the results and preparing the manuscript.

DATA AVAILABILITY

The data used are listed in the references. All equations in the numerical simulation are presented in the Methods.

COMPETING INTERESTS

The authors declare no competing interests.

REFERENCES

[1] F. A. Ochs and R. A. Lange. The density of hydrous magmatic liquids. *Science*, 283:1314–1317, 1999. doi: 10.1126/science.283.5406.1314.

[2] J. R. Holloway. *Fugacity and activity of molecular species in supercritical fluids*. Springer Netherlands, Dordrecht, Netherlands, 1977. doi: 10.1007/978-94-010-1252-2_9.

[3] L. Wilson, R. S. J. Sparks, and G. P. L. Walker. Explosive volcanic eruptions – IV. The control of magma properties and conduit geometry on eruption column behaviour. *Geophysical Journal International*, 63:117–148, 1980. doi: 10.1111/j.1365-246X.1980.tb02613.x.

[4] H. M. Gonnermann and M. Manga. The fluid mechanics inside a volcano. *Annual Review of Fluid Mechanics*, 39 (1):321–356, jan 2007. ISSN 0066-4189. doi: 10.1146/annurev.fluid.39.050905.110207.

[5] S. L. Webb and D. B. Dingwell. The onset of non-Newtonian rheology of silicate melts. *Physics and Chemistry of Minerals*, 17(2):125–132, mar 1990. ISSN 0342-1791. doi: 10.1007/BF00199663.

[6] D. B. Dingwell. Volcanic Dilemma–Flow or Blow? *Science*, 273(5278):1054–1055, 1996.

[7] H. M. Gonnermann. Magma Fragmentation. *Annual Review of Earth and Planetary Sciences*, 43(1):431–458, 2015. doi: 10.1146/annurev-earth-060614-105206.

[8] R. S. J. Sparks. The dynamics of bubble formation and growth in magmas: A review and analysis. *Journal of Volcanology and Geothermal Research*, 3(1-2):1–37, mar 1978. ISSN 03770273. doi: 10.1016/0377-0273(78)90002-1.

[9] A. Prousevitch, D. L. Sahagian, and A. T. Anderson. Dynamics of diffusive bubble growth in magmas: Isothermal case. *Journal of Geophysical Research: Solid Earth*, 98 (B12):22283–22307, dec 1993. doi: 10.1029/93JB02027.

[10] A. Toramaru. Numerical study of nucleation and growth of bubbles in viscous magmas. *Journal of Geophysical Research: Solid Earth*, 100:1913–1931, 1995. doi: 10.1029/94JB02775.

[11] O. Navon and V. Lyakhovsky. Vesiculation processes in silicic magmas. In J. S. Gilbert and R. S. J. Sparks, editors, *The physics of explosive volcanic eruptions*, pages 27–50. Geological Society, London, Special Publications, Cambridge, UK, 1998.

[12] H. Hui and Y. Zhang. Toward a general viscosity equation for natural anhydrous and hydrous silicate melts. *Geochimica et Cosmochimica Acta*, 71:403–416, 2007. doi: 10.1016/j.gca.2006.09.003.

[13] A. Toramaru. BND (bubble number density) decompression rate meter for explosive volcanic eruptions. *Journal of Volcanology and Geothermal Research*, 154:303–316, 2006. doi: 10.1016/j.jvolgeores.2006.03.027.

[14] C. Klug, K. V. Cashman, and C. Bacon. Structure and physical characteristics of pumice from the climactic eruption of Mount Mazama (Crater Lake), Oregon. *Bulletin of Volcanology*, 64:486–501, 2002. doi: 10.1007/s00445-002-0230-5.

[15] N. K. Adams, B. F. Houghton, and W. Hildreth. Abrupt transitions during sustained explosive eruptions: examples from the 1912 eruption of Novarupta, Alaska. *Bulletin of Volcanology*, 69:189–206, 2006. doi: 10.1007/s00445-006-0067-4.

[16] R. J. Carey, B. F. Houghton, and T. Thordarson. Abrupt shifts between wet and dry phases of the 1875 eruption of Askja Volcano: Microscopic evidence for macroscopic dynamics. *Journal of Volcanology and Geothermal Research*, 184:256–270, 2009. doi: 10.1016/j.jvolgeores.2009.04.003.

[17] T. Shea, L. Gurioli, J. F. Larsen, B. F. Houghton, J. E. Hammer, and K. V. Cashman. Linking experimental and natural vesicle textures in Vesuvius 79AD white pumice. *Journal of Volcanology and Geothermal Research*, 192 (1-2):69–84, apr 2010. doi: 10.1016/j.jvolgeores.2010.02.013.

[18] T. Giachetti, T.H. Druitt, A. Burgisser, L. Arbaret, and C. Galven. Bubble nucleation, growth and coalescence during the 1997 Vulcanian explosions of Soufrière Hills Volcano, Montserrat. *Journal of Volcanology and Geothermal Research*, 193(3-4), 2010. doi: 10.1016/j.jvolgeores.2010.04.001.

[19] F. Alfano, C. Bonadonna, and L. Gurioli. Insights into eruption dynamics from textural analysis: the case of the May, 2008, Chaitén eruption. *Bulletin of Volcanology*, 74:2095–2108, 2012. doi: 10.1007/s00445-012-0648-3.

[20] M. T. Mangan and K. V. Cashman. The structure of basaltic scoria and reticulite and inferences for vesiculation, foam formation, and fragmentation in lava fountains. *Journal of Volcanology and Geothermal Research*, 73(1-2):1–18, sep 1996. ISSN 03770273. doi: 10.1016/0377-0273(96)00018-2.

[21] J.D. Blower, J.P. Keating, H. M. Mader, and J.C. Phillips. The evolution of bubble size distributions in volcanic eruptions. *Journal of Volcanology and Geothermal Research*, 120(1-2):1–23, 2002. ISSN 03770273. doi: 10.1016/S0377-0273(02)00404-3.

[22] T. Shea, B. F. Houghton, L. Gurioli, K. V. Cashman, J. E. Hammer, and B. J. Hobden. Textural studies of vesicles in volcanic rocks: An integrated methodology. *Journal of Volcanology and Geothermal Research*, 190(3-4):271–289, 2010. ISSN 03770273. doi: 10.1016/j.jvolgeores.2009.12.003.

[23] H. M. Gonnermann and B. F. Houghton. Magma degassing during the Plinian eruption of Novarupta, Alaska, 1912. *Geochemistry, Geophysics, Geosystems*, 13(10):n/a–n/a, oct 2012. ISSN 15252027. doi: 10.1029/2012GC004273.

[24] T. Shea. Bubble nucleation in magmas: A dominantly heterogeneous process? *Journal of Volcanology and Geothermal Research*, 343:155–170, 2017. doi: 10.1016/j.jvolgeores.2017.06.025.

[25] S. Hajimirza, H. M. Gonnermann, and J. E. Gardner. Eruptive dynamics in plinian silicic eruptions. *EarthArXiv*, 2020.

[26] T. Giachetti, H. M. Gonnermann, J. E. Gardner, A. Burgisser, S. Hajimirza, T. C. Earley, N. Truong, and P. Toledo. Bubble Coalescence and Percolation Threshold in Expanding Rhyolitic Magma. *Geochemistry, Geophysics, Geosystems*, 20:1054–1074, 2019. doi: 10.1029/2018GC008006.

[27] K. Yamada, H. Tanaka, K. Nakazawa, and H. Emori. A new theory of bubble formation in magma. *Journal of Geophysical Research: Solid Earth*, 110(2):1–17, 2005. ISSN 21699356. doi: 10.1029/2004JB003113.

[28] S. Hajimirza, H. M. Gonnermann, J. E. Gardner, and T. Giachetti. Predicting homogeneous bubble nucleation in rhyolite. *Journal of Geophysical Research: Solid Earth*, 124:2395–2416, 2019. doi: 10.1029/2018JB015891.

[29] M. T. Mangan and T. Sisson. Delayed, disequilibrium degassing in rhyolite magma: decompression experiments and implications for explosive volcanism. *Earth and Planetary Science Letters*, 183:441–455, 2000. doi: 10.1016/S0012-821X(00)00299-5.

[30] C. C. Mourtada-Bonnefoi and D. Laporte. Homogeneous bubble nucleation in rhyolitic magmas: An experimental study of the effect of H2O and CO2. *Journal of Geophysical Research: Solid Earth*, 107(B4):ECV 2–1–ECV 2–19, 2002. doi: 10.1029/2001JB000290.

[31] H. M. Gonnermann and J. E. Gardner. Homogeneous bubble nucleation in rhyolitic melt: Experiments and nonclassical theory. *Geochemistry, Geophysics, Geosystems*, 14(11):4758–4773, 2013. doi: 10.1002/ggge.20281.

[32] P. J. Wallace, T. Plank, M. Edmonds, and E. H. Hauri. Chapter 7 - volatiles in magmas. In H. Sigurdsson, B. Houghton, S. McNutt, R. Hazel, and J. Stix, editors, *The Encyclopedia of Volcanoes (Second Edition)*, pages 163 – 183. Academic Press, Amsterdam, 2015. doi: 10.1016/B978-0-12-385938-9.00007-9.

[33] L. G. Mastin and M. S. Ghiorso. A numerical program for steady-state flow of magma-gas mixtures through vertical eruptive conduits. Technical report, Department of the Interior, Washington DC, 2000.

[34] D. Bercovici and C. Michaut. Two-phase dynamics of volcanic eruptions: Compaction, compression and the conditions for choking. *Geophysical Journal International*, 182(2):843–864, 2010. doi: 10.1111/j.1365-246X.2010.04674.x.

[35] P. J. Wallace and T. M. Gerlach. Magmatic Vapor Source for Sulfur Dioxide Released During Volcanic Eruptions: Evidence from Mount Pinatubo. *Science*, 265(5171):497–499, jul 1994. doi: 10.1126/science.265.5171.497.

[36] M. Edmonds and A. W. Woods. Exsolved volatiles in magma reservoirs. *Journal of Volcanology and Geothermal Research*, 368:13–30, 2018. ISSN 03770273. doi: 10.1016/j.jvolgeores.2018.10.018.

[37] H. M. Gonnermann, T. Giachetti, C. Fliedner, C. T. Nguyen, B. F. Houghton, J. A. Crozier, and R. J. Carey. Permeability During Magma Expansion and Compaction. *Journal of Geophysical Research: Solid Earth*, pages 1–15, 2017. ISSN 21699313. doi: 10.1002/2017JB014783.

[38] H. Massol and T. Koyaguchi. The effect of magma flow on nucleation of gas bubbles in a volcanic conduit. *Journal of Volcanology and Geothermal Research*, 143:69–88, 2005. doi: 10.1016/j.jvolgeores.2004.09.011.

[39] A. C. Rust and K. V. Cashman. Permeability controls on expansion and size distributions of pyroclasts. *Journal of Geophysical Research: Solid Earth*, 116(11):1–17, 2011. ISSN 21699356. doi: 10.1029/2011JB008494.

[40] M. Cassidy, M. Manga, K. V. Cashman, and O. Bachmann. Controls on explosive-effusive volcanic eruption styles. *Nature Communications*, 9:2839, 2018. doi: 10.1038/s41467-018-05293-3.

[41] Benjamin J. Andrews and James E. Gardner. Effects of caldera collapse on magma decompression rate: An example from the 1800 14C yrBP eruption of Ksudach Volcano, Kamchatka, Russia. *Journal of Volcanology and Geothermal Research*, 198(1-2):205–216, 2010. ISSN 03770273. doi: 10.1016/j.jvolgeores.2010.08.021.

[42] M. L. Myers, P. J. Wallace, C. J. N. Wilson, J. M. Watkins, and Y. Liu. Ascent rates of rhyolitic magma at the onset of three caldera-forming eruptions. *American Mineralogist*, 103(6):952–965, 2018. ISSN 19453027. doi: 10.2138/am-2018-6225.

[43] Y. B. Slezin. The mechanism of volcanic eruptions (a steady state approach). *Journal of Volcanology and Geothermal Research*, 122(1-2):7–50, 2003. ISSN 03770273. doi: 10.1016/S0377-0273(02)00464-X.

[44] N. Cluzel, D. Laporte, A. Provost, and I. Kannewischer. Kinetics of heterogeneous bubble nucleation in rhyolitic melts: implications for the number density of bubbles in volcanic conduits and for pumice textures. *Contributions to Mineralogy and Petrology*, 156:745–763, 2008. doi: 10.1007/s00410-008-0313-1.

[45] S. Hurwitz and O. Navon. Bubble nucleation in rhyolitic melts: Experiments at high pressure, temperature, and water content. *Earth and Planetary Science Letters*, 122:267–280, 1994. doi: 10.1016/0012-821X(94)90001-9.

[46] J. E. Gardner and M. Denis. Heterogeneous bubble nucleation on Fe-Ti oxide crystals in high-silica rhyolitic melts. *Geochimica et Cosmochimica Acta*, 68:3587–3597, 2004. doi: 10.1016/j.gca.2004.02.021.

[47] A. A. Chernov, V. K. Kedrinsky, and A. A. Pil'nik. Kinetics of gas bubble nucleation and growth in magmatic melt at its rapid decompression. *Physics of Fluids*, 26(11), 2014. ISSN 10897666. doi: 10.1063/1.4900846.

[48] M S Plesset and A Prosperetti. Bubble Dynamics and Cavitation. *Annual Review of Fluid Mechanics*, 9(1):145–185, jan 1977. ISSN 0066-4189. doi: 10.1146/annurev.fl.09.010177.001045.

[49] Y. Liu, Y. Zhang, and H. Behrens. Solubility of H_2O in rhyolitic melts at low pressures and a new empirical model for mixed H_2O–CO_2 solubility in rhyolitic melts. *Journal of Volcanology and Geothermal Research*, 143:219–235, 2005. doi: 10.1016/j.jvolgeores.2004.09.019.

[50] Y. Zhang and H. Behrens. H_2O diffusion in rhyolitic melts and glasses. *Chemical Geology*, 169:243–262, 2000. doi: 10.1016/s0009-2541(99)00231-4.

[51] J. E. Gardner, S. Hajimirza, J. D. Webster, and H. M. Gonnermann. The impact of dissolved fluorine on bubble nucleation in hydrous rhyolite melts. *Geochimica et Cosmochimica Acta*, 226:174–181, 2018. doi: 10.1016/j.gca.2018.02.013.

SUPPLEMENTARY MATERIALS

Supplementary Table 1: Experimental conditions and results. P_i and P_f are initial and final pressures, T is temperature, t_h is hydration duration, t_d is decompression time, t_p is sample hold time before quench, [H_2O] is dissolved water concentration and N_m is bubble number density. [a]Experiments were discussed in Gonnermann and Gardner [31]. [b]Experiments were discussed in Hajimirza et al. [28]. [c]Experiments were discussed in Giachetti et al. [26]. [d]Experiments were discussed in Gardner et al. [51]. [e] Outliers. 5 out of 35 decompression experiments are considered as outliers because they have a considerably different N_m comparing to N_m in experiments within the same suite.

Run	Sarting material	P_i (MPa)	P_f (MPa)	T (°C)	t_h (hr)	t_d (s)	t_{post} (s)	[H_2O] (wt%)	N_m (m^{-3})
Hydration experiments									
G-885[a]	Rhyolite	160	160	875	120	-	-	5.00 ± 0.01	-
G-595[a]	Rhyolite	160	160	875	120	-	-	4.93 ± 0.13	-
G-1594A[b]	Rhyolite	160	160	875	118	-	-	4.79 ± 0.01	-
G-1607[b]	Rhyolite	160	160	875	121	-	-	4.85 ± 0.08	
G-876[a]	Rhyolite	160	160	875	120	-	-	5.08 ± 0.01	-
G-1780	Rhyolite	160	160	850	173	-	-	5.02 ± 0.13	-
G-1770	Rhyolite	190	190	850	173	-	-	6.03 ± 0.09	-
G-1771	Rhyolite	190	190	850	173	-	-	6.01 ± 0.11	-
G-1570	Rhyolite	190	190	850	168	-	-	5.53 ± 0.01	-
G-1579	Rhyolite	190	190	850	168	-	-	5.45 ± 0.11	-
G-1731	Rhyolite	190	190	850	169	-	-	5.69 ± 0.06	-
G-1736	Rhyolite	190	190	850	163	-	-	–	-
G-1779	Rhyolite	190	190	850	168	-	-	5.68 ± 0.02	-
G-1778	Rhyolite	190	190	850	168	-	-	5.91 ± 0.09	-
G-1594B[b]	Rhyolite	200	200	875	118	-	-	5.51 ± 0.03	-
G-1608[c]	Rhyolite	200	200	875	123	-	-	5.48 ± 0.04	-
G-1457[c]	Rhyolite	200	200	850	144	-	-	5.71 ± 0.02	-
G-1456[c]	Rhyolite	200	200	850	145	-	-	5.70 ± 0.01	-
G-1483[c]	Rhyolite	200	200	850	216	-	-	5.50 ± 0.08	-
G-1608[c]	Rhyolite	200	200	850	123	-	-	5.48 ± 0.04	-
G-1680[d]	Rhyolite	250	250	850	167	-	-	6.45 ± 0.08	-
G-1591[d]	Rhyolite	250	250	850	167	-	-	–	-
G-1732	Rhyolite	250	250	850	172	-	-	6.45 ± 0.08	-
G-1742	Rhyolite	250	250	850	165	-	-	6.90 ± 0.06	-
G-1741[d]	Rhyolite	250	250	850	159	-	-	7.30 ± 0.7	-
Decompression experiments									
G-1614[b]	G-1594A	161	13	875	-	10	0	-	1.0×10^9
G-1616[b], [e]	G-1594A	161	11	875	-	15	5	-	1.1×10^9
G-1627[b]	G-1607	161	13	875	-	16	18	-	1.1×10^{10}
G-1628[b]	G-1607	161	11	875	-	11	29	-	2.7×10^{10}
G-1796	G-1780	161	11	875	-	11	60	-	7.1×10^9
G-608[a]	G-595	161	13	875	-	11	109	-	3.2×10^{10}
G-1746	G-1736	190	60	850	-	54	0	-	2.4×10^8
G-1776	G-1771	190	58	850	-	48	9	-	9.4×10^8
W-6	G-1731	190	60	850	-	47	10	-	9.9×10^8
G-1794	G-1731	190	60	850	-	44	22	-	1.5×10^9
W-7[e]	G-1570	190	60	850	-	55	25	-	3.4×10^{10}
G-1798	G-1779	190	59	850	-	40	23	-	1.3×10^9
G-1799	G-1779	190	59	850	-	50	30	-	2.8×10^9
G-1793	G-1778	190	60	850	-	47	44	-	2.5×10^9
W-8[e]	G-1579	190	60	850	-	55	50	-	8×10^8
G-1747	G-1736	190	46	850	-	3	0	-	4.8×10^9
W-9[e]	G-1579	190	46	850	-	3	10	-	3×10^9
G-1777	G-1771	190	42.5	850	-	2	15	-	4.4×10^{11}
G-1774	G-1770	190	42.5	850	-	2	21	-	6.2×10^{11}
G-1775	G-1770	190	42	850	-	1	41	-	6.9×10^{11}
W-10	G-1731	190	46	850	-	3	50	-	1×10^{12}
G-1617[b]	G-1594B	201	75	875	-	45	0	-	1.0×10^8
G-1620[b]	G-1594B	201	74	875	-	28	12	-	8.0×10^8
G-1148[a]	G-1594B	201	74	875	-	35	25	-	5.9×10^9
G-1622[b]	G-1594B	201	75	875	-	34	29	-	1.4×10^9
G-1632[b]	G-1608	201	75	875	-	34	56	-	2.3×10^{10}
G-1481[c]	G-1457	201	54	850	-	2	15	-	1.2×10^{12}
G-1501[c]	G-1483	201	54.0	850	-	1	31	-	2.6×10^{12}
G-1482[c]	G-1457	201	54	850	-	1	60	-	2.6×10^{12}
G-1484[c]	G-1456	201	54	850	-	2	90	-	3.4×10^{12}
G-1791	G-1741	251	134	850	-	2	40	-	0
G-1685[d]	G-1680	251	135	850	-	2	58	-	2.1×10^9
G-1797	G-1742	251	133	850	-	3	71	-	7.1×10^8
W-1[e]	G-1591	251	135	850	-	3	87	-	2.9×10^{10}
W-2	G-1732	251	135	850	-	2	118	-	1.1×10^9

Supplementary Table 2: Nucleation rate and time scale predicted for each experimental suite.

Experimental suite	P_i (MPa)	P_f (MPa)	J_s ($m^{-3}s^{-1}$)	τ_n (s)	$N_{m,final}$
1	200	54	9.5×10^{10}	33	2.8×10^{12}
2	190	42-46	2.5×10^{10}	57	1.3×10^{12}
3	160	10-13	3.5×10^{8}	319	9.9×10^{10}
4	200	74-75	1.2×10^{8}	482	5.1×10^{10}
5	190	58-60	6.4×10^{7}	628	3.5×10^{10}
6	250	132-135	1.5×10^{7}	1120	1.5×10^{10}

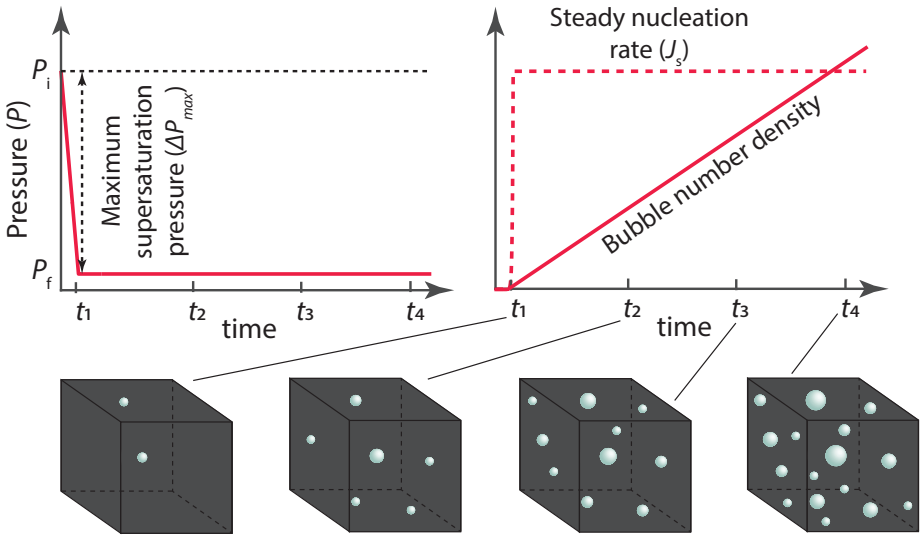

Supplementary Figure 1: Supplementary: Schematic representation of bubble nucleation in during experiments. Samples within a given suite have similar initial and final pressures as well as decompression rates, but are quenched at different times. At the final pressure nucleation continues while the sample remains supersaturated. As a consequence bubble number density increases proportionally to annealing time.

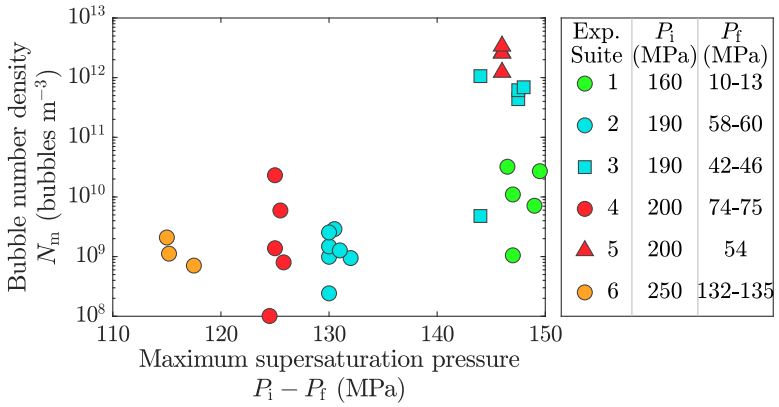

Supplementary Figure 2: Supplementary: Observed bubble number density in experiments as a function of supersaturation pressure. For each experimental suite, characterized by similar decompression and decompression rate, bubble number density varies considerably, in some suites over more than 2 orders of magnitude.

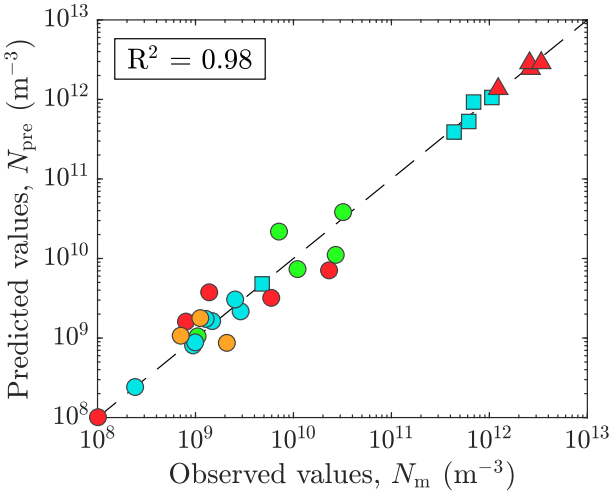

Supplementary Figure 3: Supplementary: Predicted bubble number densities compared with the observed values. The predicted values are from equation 30 in the main text. The dashed line represents 1:1 line. All predicted values are within one order of magnitude of observed bubble number densities.